Taylor & Francis
Taylor & Francis Group

Check for updates

A computational study of mucociliary transport in healthy and diseased environments

Hanliang Guo and Eva Kanso

Department of Aerospace and Mechanical Engineering, University of Southern California, Los Angeles, CA, USA

ABSTRACT

Mucociliary clearance is the primary defense mechanism that protects the airways from inhaled toxicants and infectious agents. The fluid medium is spatially non-homogenous, consisting of a viscoelastic mucus layer on top of a nearly-viscous periciliary layer surrounding the motile cilia. In healthy environments, the thickness of the periciliary layer is comparable to the cilia length. Perturbations to this system are directly linked to infection and disease. Clinical evidence links the periciliary layer depletion to reduced rates of mucus clearance. Here, we develop a computational model to systematically study the effects of the viscoelastic properties and thickness of the mucus layer on the system's performance. We find that, compared to a control case with no mucus, a healthy mucus layer enhances the cilia performance: it improves flow transport at an energetic advantage to the cilia. In contrast, when the periciliary layer is depleted, mucus hinders transport and stiffer mucus leads to a substantial decrease in transport efficiency. This decrease in transport is accompanied by an increase in the cilia internal forces and power needed to complete the cilia beating cycle. We conclude by commenting on the relevance of these findings to understanding mucociliary transport in healthy and diseased environments.

1. Introduction

Fluid transport in confined microenvironments is an essential process in many biological and engineered systems (Brennen & Winet, 1977; Zhao, Moore, & Beebe, 2001; Simonnet & Groisman, 2005; Fauci & Dillon, 2006). In the mammalian body for example, particle- and cell-laden fluid is transported by motile cilia – active slender filaments – found on the epithelial cells of the upper airways (Fulford & Blake, 1986; O'Callaghan, Sikand, & Rutman, 1999; Randell & Boucher, 2006), ependymal cells in the brain (Del Bigio, 1995; Mirzadeh, Han, Soriano-Navarro, García-Verdugo, & Alvarez-Buylla, 2010) and cells lining the oviduct and epididymis of the reproductive tracts (Lyons, Saridogan, & Djahanbakhch, 2006). In engineered microfluidic devices, several techniques

---

CONTACT Eva Kanso ✉ kanso@usc.edu

have been devised for fluid and particle transport and manipulation (Stone, Stroock, & Ajdari, 2004), including micron-scale magnetically actuated tails (Dreyfus et al., 2005; Tierno, Golestanian, Pagonabarraga, & Sagués, 2008) and synthetic molecular rotors (Van Delden et al., 2005; Eelkema et al., 2006). This technologies are enabling the fabrication of arrays of active filaments that beat synchronously and transport fluids in microfluidic channels (Kirby, 2010; Mark, Haeberle, Roth, von Stetten, & Zengerle, 2010; Khaderi et al., 2011). Simulations of synthetic cilia are also carried out for motion regulations of microparticles (Masoud & Alexeev, 2011). In many of these biological and technological applications, the fluid that needs to be transported exhibit spatially-inhomogeneous viscoelastic properties (Lauga, 2007; Smith, Gaffney, & Blake, 2008). This work is particularly concerned with mucociliary clearance in the lung.

The mucociliary clearance system consists of two components: a viscoelastic mucus layer that traps inhaled particles and gets transported out of the lung by cilia-generated forces, and a low-viscosity periciliary layer that facilitates the beating of cilia; see Figure 1(a). Mucus clearance is the primary defense mechanism that protects the airways from inhaled toxicants and infectious agents (Cone, 2009; Boucher, 2007). Failure of mucus clearance is linked to human lung diseases such as chronic obstructive pulmonary disease (COPD) (Del Donno, Bittesnich, Chetta, Olivieri, & Lopez-Vidriero, 2000; Rogers, 2004; Rogers, 2005; Hogg, 2004; Comer et al., 2012; Seys et al., 2015) and cystic fibrosis (CF) (Boucher, 2007; Livraghi & Randell, 2007; Wielpütz et al., 2013). Great advances have been made in understanding the mechanics of ciliary transport and cilia-generated flows; see, for example, Chopra, Taplin, Simmons, and Elam (1977), Smith et al. (2008), Smith, Gaffney, and Blake (2009), Li et al. (2012) and Ding, Nawroth, McFall-Ngai, and Kanso (2014). However, there is a shortage of quantitative models that predict the degree of failure in mucus transport under perturbed and diseased conditions (Davenport & Yoder, 2005; Brooks & Wallingford, 2014; Figure 1(b). Predictive airway clearance models would improve the understanding of cilia-related lung diseases and the development of treatment therapies (Boucher, 2004; Wanner, Salathé, & O'Riordan, 1996; Button et al., 2012).

Early mathematical models of mucociliary transport date back to the work of Barton & Raynor (1967). The authors considered the cilium to be a rigid rod that is shorter during the recovery stroke than during the effective stroke, and approximated its effect on the surrounding fluid using 'resistance' coefficients that allowed them to obtain somewhat realistic flow rates (Barton & Raynor, 1967). Numerous studies were conducted thereafter, shedding more light on the mechanics of mucociliary transport; see, for example, Fulford & Blake (1986), Smith et al. (2008), Lee et al. (2011), Jayathilake, Tan, Le, Lee, and Khoo (2012), Montenegro-Johnson, Smith, and Loghin (2013), Jayathilake, Le, Tan, Lee, and Khoo (2015), Li, Favier, D'Ortona, and Poncet (2016) and Chatelin & Poncet

(2016) and references therein. Most of these works consider single or two-layer Newtonian fluids, focusing on the effects of difference in viscosity between the two layers on fluid transport. Viscoelastic properties of the mucus were first taken into account by Ross (1971). Ross considered a Maxwell fluid propelled by a continuous 'wavy wall' and analytically solved for the fluid transport rates (Ross, 1971). More recently, Smith, Gaffney, and Blake (2007) proposed a traction layer model consisting of three layers: a periciliary layer of Newtonian fluid, a mucus layer of Maxwell fluid, and a thin traction layer between the periciliary and mucus layers accounting for the interaction between the cilia and the mucus. The effect of cilia beating is modeled as a time-dependent force acting on the traction layer (Smith et al., 2007). The traction-layer model predicts physiologically-reasonable values of mucus transport and provides great insight into the temporal and spatial details of mucociliary flows. However, it is limited in that it cannot take into account the details of specific cilia beating patterns. It is also limited by the Maxwell fluid assumption, which is a linear model of viscoelasticity. In the same year, Mitran (2007) developed a discrete computational framework for mucociliary transport that considers a two-layer fluid: a viscoelastic mucus layer on top of a Newtonian periciliary layer, and prescribed the internal forces along the cilia (Mitran, 2007). He showed the emergence of metachronal waves due to hydrodynamic coupling and noted that the metachronal beating of cilia is energetically beneficial. Note that in all these works, the periciliary fluid layer was considered Newtonian but recent investigations suggest that this view may be too simplistic and that the periciliary layer possesses viscoelastic properties (Tarran et al., 2001; Button et al., 2012).

In this paper, we present a mucociliary transport model consisting of two fluid layers: a mucus layer of highly viscoelastic fluid on top of a periciliary layer of nearly viscous fluid, as in the case of biological ciliary systems Boucher (2004). We account for the viscoelastic effects using the Oldroyd-B fluid model Larson (1999). The Oldroyd-B model, despite its simplicity, captures the main mechanical features of viscoelastic fluids under shear conditions, that is to say, under conditions that are reminiscent to the shearing motions produced by beating cilia. We formulate a system of equations governing fluid-cilia interactions and solve it numerically using the immersed boundary method (IBM) first proposed by Peskin (1972) to study flow around heart valves (Peskin, 1972; Peskin, 2002) and later developed and applied successfully to various fluid–structure interaction problems including problems involving non-Newtonian fluids (Dillon, Fauci, Omoto, & Yang, 2007; Teran, Fauci, & Shelley, 2010; Chrispell, Cortez, Khismatullin, & Fauci, 2011; Thomases & Guy, 2014).

We make several simplifications for the sake of developing a tractable computational model that allows us to systematically probe the effects of the periciliary layer thickness and mucus properties on the transport performance:
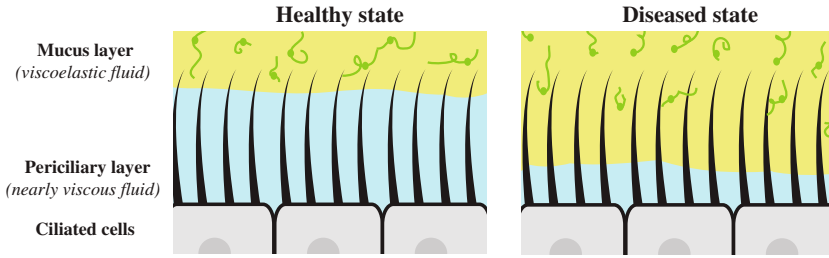
Figure 1. Healthy and diseased ciliary systems. In a healthy state, cilia lie mostly in a nearly-viscous periciliary layer, with only the tips penetrating into the viscoelastic mucus layer. In a diseased state, the mucus is denser and thicker, submerging the cilia in a mostly viscoelastic environment.

(i) The beating pattern of the filament is constructed from the rabbit tracheal cilia (Fulford & Blake, 1986). We assume that the beating kinematics is not affected by the thickness of the mucus layer or its elastic properties. This assumption is useful to compare the performance – internal forces, power and efficiency – of the unchanged cilia kinematics under various mucus conditions, but it does not allow the beat kinematics to change dynamically in response to changes in the fluid environment.

(ii) Viscoelastic effects are modeled using the Oldroyd-B fluid model (Larson, 1999). The Oldroyd-B model captures the main mechanical features of viscoelastic fluids under shear conditions, that is to say, under conditions that are reminiscent to the shearing motions produced by beating cilia, but it does not include shear thinning effects.

(iii) Previous experimental and numerical works have shown that the interface between the mucus and periciliary layers exhibits no significant deformations under the effect of cilia beating (Sanderson & Sleigh, 1981; Smith et al., 2008; Dillon et al., 2007). We therefore assume no deformation at the interface and match the elastic component of the shear stress at the interface between the periciliary and mucus layers.

(iv) In mucociliary transport, the periciliary and mucus layers have distinct viscosities, with typical values of the order $\mu = 10^{-3}$Pa·s for the periciliary layer and $\mu = 10^{-1}$Pa·s for the mucus layer. Several studies have focused on the effect of this difference in viscosity on fluid transport (Fulford & Blake, 1986; Lee et al., 2011). Our goal here is to isolate and examine the viscoelastic effects on fluid transport, thus we set both viscosities to be the same.

(v) We formulate the equations of motion governing the fluid-filament interactions using the Navier–Stokes equations and solve them numerically using the IBM pioneered by Peskin (1972), Peskin (1972) and Peskin (2002) and later extended to non-Newtonian fluids (Dillon et al., 2007; Teran et al., 2010; Chrispell et al., 2011; Thomases & Guy, 2014). The Reynolds number based on the length of the filament and its beating frequency is defined as Re $= \rho l^2/\mu T$, where ρ and μ are fluid density
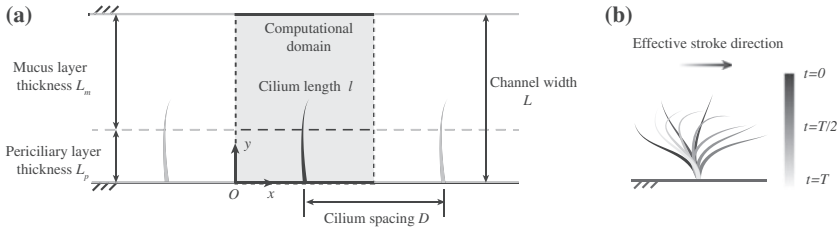
Figure 2. Model schematics. (a) an infinite array of motile cilia beating synchronously in a channel. The channel is filled with a viscoelastic fluid of thickness L_m atop a nearly viscous fluid of thickness L_p. (b) Kinematics of rabbit tracheal cilia, based on Fulford & Blake (1986) and scaled to preserve the length of the cilium. The effective stroke is shown in dark grey and the recovery stroke in light grey.

and viscosity and l and T are the cilium length and beating frequency, with typical values $l = 10\,\mu\text{m}$, $T = 0.1\text{s}$, $\rho = 10^3\,\text{kg}\cdot\text{m}^{-3}$, $\mu = 10^{-3}\text{Pa}\cdot\text{s}$. For these parameter value, one gets $\text{Re} = 10^{-3}$, hence inertia is negligible and one could use the Stokes equations to model the system. The IBM approach for one-way coupled systems in Stokes flow tends to be numerically stiff (Teran & Peskin, 2009). Therefore, we use the one-way coupled IBM for Navier–Stokes equations proposed in Taira & Colonius (2007) and embed a viscoelastic solver for the Oldroyd-B model with a finite but small Reynolds number $\text{Re} = 0.1$, which we view as a numerical 'regularization' parameter to reduce the computational cost. Smaller Reynolds numbers lead to results that are qualitatively similar but at a much higher computational cost. To quantify the difference introduced by the finite Reynolds number, one can use the analytical solution to Taylor's swimming sheet (Taylor, 1951) as a proxy and compare it with the computational solution with finite Reynolds number. Here we refer to Chrispell et al. (2013) where they showed the difference in swimming velocity between the numerical simulations for $\text{Re} = 0.1$ and the analytical solution for $\text{Re} = 0$ is minimal for Newtonian fluid. For viscoelastic fluid, the numerical results for $\text{Re} = 0.1, \text{De} = 1$ agrees well with Lauga's asympotics (Lauga, 2007) at small amplitudes for $\text{Re} = 0, \text{De} = 1$. For larger amplitudes, the numerical results for finite Reynolds number are about 30% lower than those of the asymptotics.

We use this computational framework to conduct a systematic study of the effects of the parameters of the mucus layer on mucociliary transport. In particular, we vary the mucus properties and thickness to emulate a range of healthy and diseased conditions. Our findings suggest that the mucus parameters greatly affect mucociliary transport. We conclude by discussing the significance of these results in relation to mucociliary transport in healthy and diseased conditions, as well as the design of microfluidic transport mechanisms for biological and artificial cilia.

2. Model and method

2.1. Problem formulation

Consider an infinite array of cilia beating in synchrony in a narrow channel of width L. The cilia have length l and are uniformly distributed on one side of the channel at a separation distance D as shown in Figure 2(a). The channel is filled with two fluid layers: a viscoelastic mucus layer of thickness L_m on top of a nearly-viscous periciliary layer of thickness L_p, with $L_p + L_m = L$.

The cilia beating kinematics are based on experimental data of the rabbit tracheal cilia Fulford & Blake (1986) and depicted in Figure 2(b). Mathematically, the beating kinematics can be described in a Cartesian frame (x, y) attached at the base of the cilium using the vector representation $\boldsymbol{\xi}_c(s, t)$, where s is the arclength along the cilium's centreline from its base ($0 < s < l$) and t is time ($0 < t < T$). The (x_c, y_c) components of $\boldsymbol{\xi}_c(s, t)$ are given by a Fourier series expansion in t and Taylor series in s with coefficients chosen to match the experimental data. It should be noted that the cilium length is not conserved by the coefficients reported in Fulford & Blake (1986). Here, we rescaled the coefficient to ensure the total length of the cilium is constant at all time.

The mucus and periciliary layers are described using the Oldroyd-B model for polymeric fluids, that is to say, for fluids consisting of a viscous fluid solvent and a polymeric elastic solute (Larson, 1999). The total deviatoric stress $\boldsymbol{\sigma} = \boldsymbol{\sigma}_f + \boldsymbol{\sigma}_e$ of the Oldroyd-B fluid consists of contributions from the Newtonian fluid solvent $\boldsymbol{\sigma}_f$ and the polymeric elastic solute $\boldsymbol{\sigma}_e$. The constitutive stress–strain relations are given by

$$\boldsymbol{\sigma}_f = 2\mu_f \boldsymbol{D}(\boldsymbol{u}), \qquad \boldsymbol{\sigma}_e + r\boldsymbol{\sigma}_e^{\triangledown} - 2\mu_e \boldsymbol{D}(\boldsymbol{u}) - \epsilon\nabla^2\boldsymbol{\sigma}_e = \boldsymbol{0}, \tag{1}$$

where $\boldsymbol{D}(\boldsymbol{u}) = \frac{1}{2}[\nabla\boldsymbol{u} + (\nabla\boldsymbol{u})^T]$ is the strain rate tensor, r is the relaxation time of the viscoelastic fluid, $(\,\cdot\,)^{\triangledown} \equiv \frac{\partial}{\partial t}(\,\cdot\,) + \boldsymbol{u}\cdot\nabla(\,\cdot\,) - [\nabla\boldsymbol{u}(\,\cdot\,) + (\,\cdot\,)(\nabla\boldsymbol{u})^T]$ denotes the upper convected derivative, μ_f and μ_e are the viscosities of the fluid solvent and elastic solute respectively. The relaxation time of the viscoelastic material describes the time required for the elastic polymers in the fluid to return to equilibrium after the stress is released (Larson, 1999). Informally, it could also be understood as 'the duration for which the material remembers the effect of an applied force'. Larger r means that applied forces will remain effective for a longer time after unloading. It should be noted that the diffusion term $\epsilon\nabla^2\boldsymbol{\sigma}_e$ is not inherent to the constitutive relation of the Oldroyd-B model. It has been added as a regularization term with $\epsilon \ll 1$ because, in its absence, the stress tensors of the Oldroyd-B model have the potential to lose smoothness in the long-time limit (Thomases, 2011; Thomases & Guy, 2014). We validate our choice of ϵ by systematically decreasing ϵ and making sure the results are consistent, as discussed in Section 2.2.

Table 1. Dimensional and dimensionless fluid parameters. Dimensionless parameters are scaled by the cilia length l, the period of the beating cycle T, and the total viscosity $\mu = \mu_e + \mu_f$. In this study, we vary the shaded parameters while keeping all other parameters fixed.

	Periciliary layer		Mucus layer	
	Dimensional	Dimensionless	Dimensional	Dimensionless
Layer thickness	L_p	L_p	$L_m = L - L_p$	$L_m = L - L_p$
Relaxation time	r_p	$\mathrm{De}_p = 0.05$	r_m	De_m
Viscosity of elastic solute	μ_e	$\alpha = 0.5$	μ_e	$\alpha = 0.5$
Viscosity of fluid solvent	μ_f	$1 - \alpha = 0.5$	μ_f	$1 - \alpha = 0.5$
Total viscosity	$\mu = \mu_e + \mu_f$	1	$\mu = \mu_e + \mu_f$	1

The equations of motion of the Oldroyd-B fluid are obtained by substituting the regularized constitutive relations into the balance of linear momentum. To this end, one gets the modified Navier–Stokes equation:

$$\rho\left(\frac{\partial \boldsymbol{u}}{\partial t} + \boldsymbol{u}\cdot\nabla\boldsymbol{u}\right) + \nabla p - \mu_f\nabla^2\boldsymbol{u} - \nabla\cdot\boldsymbol{\sigma_e} - \boldsymbol{f} = \boldsymbol{0}. \tag{2}$$

Here, ρ is the fluid density, p is the pressure field and $\boldsymbol{f}$ is the body force density acting on the fluid. Equation (2) is to be solved in the fluid channel in conjunction with the incompressibility equation $\nabla \cdot \boldsymbol{u} = 0$ and the constitutive equation for $\boldsymbol{\sigma}_e$ from (1). The solution to this coupled system of equations should satisfy the no-slip boundary conditions at the channel walls and along the individual cilia

$$\boldsymbol{u} = \begin{cases} \dfrac{\partial \boldsymbol{\xi}_c}{\partial t} & \text{at the cilia,} \\ \boldsymbol{0} & \text{on the channel walls: } y = 0 \text{ and } y = L. \end{cases} \tag{3}$$

To emulate the effect of the mucus layer on top of the periciliary layer, we consider two viscoelastic fluids of different material properties. The mucus layer consists of a viscoelastic fluid of thickness L_m and longer relaxation time r_m. The mucus layer lies on top of a nearly-viscous periciliary fluid of thickness L_p and shorter relaxation time r_p. Previous experimental and numerical works have shown that the interface between the mucus and periciliary layers exhibits no significant deformations under the effect of cilia beating (Sanderson & Sleigh, 1981; Smith et al., 2008; Dillon et al., 2007). We therefore assume no deformation at the interface. This assumption means that only the solvent could be exchanged between the periciliary and mucus layers but not the polymer molecules which dictate the relaxation time of the viscoelastic fluids (Randell & Boucher, 2006; Button et al., 2012). Mathematically, the fluid velocities are continuous at the interface and the extra shear stress $\boldsymbol{\sigma}_e$ is zero, $\boldsymbol{\sigma}_e|_{y=L_p} = 0$. This is based on the fact that the periciliary layer has small elastic component ($r_p/r_m \ll 1$), thus the elastic stress at the interface is close to zero.

We use the cilium length l to scale length, the beating cycle T to scale time, the total viscosity $\mu = \mu_f + \mu_e$ to scale viscosity, and the ratio between the

total viscosity of the fluid to the beating cycle μ/T to scale pressure. A summary of the dimensional and dimensionless parameters can be found in Table 1. The non-dimensional thickness of the fluid layers in the channel are $L_p \equiv L_p/l$ and $L_m \equiv L_m/l$. The fluid is characterized by three non-dimensional parameters: (i) the Reynolds number $\mathrm{Re} = \rho l^2/\mu T$ measures the ratio of inertial to viscous effects and, therefore, is negligible in drag-dominant flows – here, we set $\mathrm{Re} = 0.1$ for numerical reasons as mentioned earlier; (ii) the Deborah number $\mathrm{De} = r/T$ measures the elastic properties of the viscoelastic fluid and takes two distinct values: De_m in the mucus layer and De_p in the periciliary layer – here, we fix De_p and vary De_m; and (iii) the ratio of elastic to total viscosity $\alpha = \mu_e/\mu$, which we take to be the same in the mucus and periciliary layers. In non-dimensional form, Equation (2) and the incompressibility condition are written as

$$\mathrm{Re}(\frac{\partial \boldsymbol{u}}{\partial t} + \boldsymbol{u}\cdot\nabla\boldsymbol{u}) + \nabla p - (1-\alpha)\nabla^2\boldsymbol{u} - \nabla\cdot\boldsymbol{\sigma_e} - \boldsymbol{f} = \boldsymbol{0},$$

$$\nabla\cdot\boldsymbol{u} = 0.$$

(4)

These equations are coupled to the constitutive relations for $\boldsymbol{\sigma}_e$ from Equation (1), which in non-dimensional form are given by

$$\mathrm{De}_p\,\boldsymbol{\sigma}_e^{\nabla} + \boldsymbol{\sigma}_e - 2\alpha\,\boldsymbol{D}(\boldsymbol{u}) - \epsilon\nabla^2\boldsymbol{\sigma}_e = \boldsymbol{0}, \qquad \text{for } 0 \leq y < L_p,$$

$$\mathrm{De}_m\boldsymbol{\sigma}_e^{\nabla} + \boldsymbol{\sigma}_e - 2\alpha\,\boldsymbol{D}(\boldsymbol{u}) - \epsilon\nabla^2\boldsymbol{\sigma}_e = \boldsymbol{0}, \qquad \text{for } L_p \leq y < L.$$

(5)

The set of Equations (4) and (5) reduce to the typical incompressible Navier–Stokes equations when $\mathrm{De}_p = \mathrm{De}_m = 0$, $\alpha = 0$, and $\epsilon = 0$.

2.2. Numerical method

For viscous fluids ($\boldsymbol{\sigma}_e \equiv \boldsymbol{0}$) and fixed boundaries, the incompressible Navier–Stokes Equation (4) can be discretized using a standard fluid solver, such as the classical fractional step method where pressure p is treated as a Lagrange multiplier to ensure the fluid velocities satisfy the incompressibility condition (Chorin, 1968; Chang, Giraldo, & Perot, 2002; Fletcher, 2012). In the case of moving boundaries, a standard numerical method for solving Equation (4) is the IBM Peskin (1972, 2002). IBM uses a standard Eulerian (fixed) mesh to solve for the fluid velocity field and a Lagrangian (moving) mesh to account for the moving boundary, here, the cilium. To communicate between these two meshes, a regularized Dirac delta function δ is used to project the boundary forces $\boldsymbol{F}$ onto the fluid domain,

$$\boldsymbol{f}(\boldsymbol{x}, t) = \int_{\mathcal{C}} \boldsymbol{F}(\boldsymbol{\xi}, t)\delta(\boldsymbol{x} - \boldsymbol{\xi}(s, t))\mathrm{d}s,$$

(6)

and to project the fluid velocities $\boldsymbol{u}$ onto the moving boundary,

$$\frac{\partial \boldsymbol{\xi}(s, t)}{\partial t} = \int_{\mathcal{F}} \boldsymbol{u}(\boldsymbol{x}, t)\delta(\boldsymbol{x} - \boldsymbol{\xi}(s, t))\mathrm{d}\boldsymbol{x}.$$

(7)
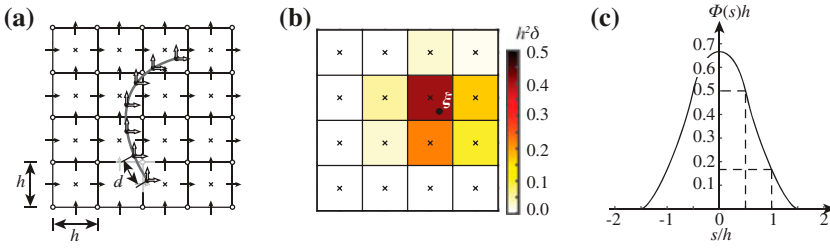
Figure 3. Numerical Methods. (a) Staggered Eulerian mesh: the horizontal and vertical arrows $(\rightarrow, \uparrow)$ represent the discrete velocities in x, y directions respectively. The pressure p and the normal stresses σ_{11}, σ_{22} are located at the cell centers $(\times)$. The shear stress σ_{12} are located at the cell corners $(\circ)$. The Lagrangian boundary points are represented by filled circles $(\bullet)$. The discrete forces along the boundary are represented by thick arrows $(\Rightarrow, \Uparrow)$. (b) The regularized Dirac delta function $\delta(\boldsymbol{x}(x,y) - \boldsymbol{\xi}(\xi, \eta)) = \phi(x - \xi)\phi(y - \eta)$ evaluated at the Eulerian mesh, where ϕ is a one-dimensional regularized Dirac delta function. (c) Here, we use the function ϕ employed by Roma et al. (1999).

Here, $\mathcal{C}$ denotes the Lagrangian cilia boundary and $\mathcal{F}$ the Eulerian fluid domain. It should be emphasized that $\boldsymbol{\xi}$ and $\boldsymbol{F}$ are the Lagrangian mesh markers and force density along $\mathcal{C}$. When the motion of the boundary is unconstrained, $\boldsymbol{\xi}$ and $\boldsymbol{F}$ are typically related via an elastic energy function E such that $\boldsymbol{F}(\boldsymbol{\xi}, t) = \partial E / \partial \boldsymbol{\xi}$. In this work, the cilium $\mathcal{C}$ is constrained to follow prescribed beating kinematics $\boldsymbol{\xi}_c(t)$. A typical technique to link $\boldsymbol{\xi}(t)$ to $\boldsymbol{\xi}_c(t)$ is to impose $\boldsymbol{F}(\boldsymbol{\xi}, t) = K[\boldsymbol{\xi}_c(t) - \boldsymbol{\xi}(t)]$ and use large values of the stiffness parameter K to guarantee that the motion of the boundary $\boldsymbol{\xi}$ is close to the prescribed motion $\boldsymbol{\xi}_c$. However, this technique renders the equations of motion stiff and therefore prohibits the use of large time steps. Similar difficulties are encountered in the one-way coupled IBM for Stokes flow (Teran & Peskin, 2009).

To circumvent these difficulties, we use the one-way coupled IBM proposed in Taira & Colonius (2007), where the boundary forces $\boldsymbol{F}$ are treated as a Lagrange multiplier to ensure that the no-slip conditions $\boldsymbol{\xi} = \boldsymbol{\xi}_c$ at the cilia are satisfied. This method solves for the boundary forces $\boldsymbol{F}$ implicitly with no need for additional constitutive relationship between $\boldsymbol{\xi}$ and $\boldsymbol{F}$. The one-way coupled IBM is comparable in temporal stability to the classical fractional step method, thus enabling simulations with larger time steps (Taira & Colonius, 2007).

We embed a viscoelastic solver for the Oldroyd-B fluid Equations (4), (5) in the one-way coupled IBM. To this end, we discretize the doubly-periodic fluid domain $\mathcal{F} = [0, D] \times [0, L]$ using a uniform, finite-volume, staggered Eulerian mesh, of mesh size h. Details of the staggered mesh are shown in Figure 3(a). At each time step, we explicitly update the elastic stress tensors $\boldsymbol{\sigma}_e$ in (5) using a standard second-order Runge–Kutta scheme. Then, we substitute the updated stress tensors in the momentum Equation (4) to update the flow field $\boldsymbol{u}$, subject to the incompressibility condition $\nabla \cdot \boldsymbol{u} = 0$ and no-slip boundary
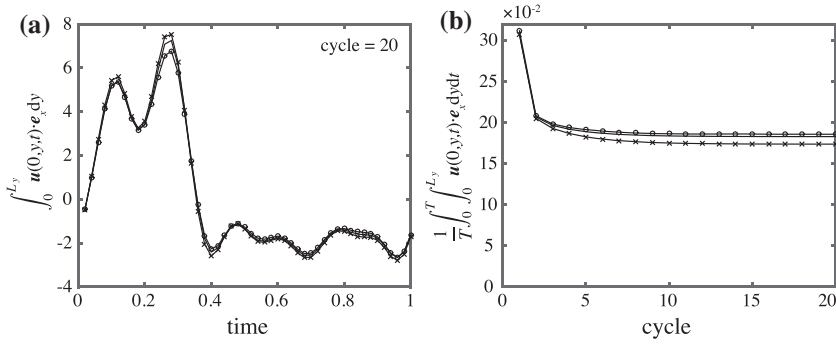
Figure 4. Numerical Convergence. (a) The flow rate within the 20th cycle. (b) The mean flow rate as a function of cycles. The Deborah number of the mucus layer is $De_m = 5$, the periciliary layer thickness is $L_p = 0.8$. '$-$': $h = 0.0156$, $\Delta t = 2 \times 10^{-5}$; '$\times$': $h = 0.0312$, $\Delta t = 2 \times 10^{-5}$; '$\circ$': $h = 0.0156$, $\Delta t = 4 \times 10^{-5}$.

conditions (3) using a fractional step method. In (4), we discretize the convective term $\boldsymbol{u} \cdot \nabla \boldsymbol{u}$ using the explicit second-order Adams–Bashforth scheme and the diffusion term $\nabla^2 \boldsymbol{u}$ using the implicit Crank–Nicolson scheme. The temporal and spatial discretization of Equations (3) and (4) yields an algebraic system of equations for the fluid velocity $\boldsymbol{u}$.

The cilium base point is located at $(x, y) = (D/2, 0)$ and the effective stroke is pointing in the positive x-direction as shown in Figure 2(b). We use the mesh size $d = h$ to discretize the cilium, as recommended by Taira & Colonius (2007) to ensure no penetration of streamlines. To communicate between the fluid domain and the moving cilia boundary, i.e. between the Eulerian and Lagrangian meshes, we discretize the Dirac delta function in (6) and (7) using the discrete Dirac delta function developed by Roma, Peskin, and Berger (1999) and illustrated in Figure 3(b) and (c). The forces $\boldsymbol{F}$ and fluid velocity $\boldsymbol{u}$ are updated simultaneously at each time step.

We let the fluid domain $\mathcal{F}$ be of size $D \times L = [0, 2] \times [0, 2]$, and we set the total integration time to be 20 cilia-beating cycles. The numerical values of the mesh sizes $h = d = 0.0156$ and the timestep $\Delta t = 2 \times 10^{-5}$ are chosen so that the solution changes little under further spatial and temporal mesh refinement. In particular, a decrease in the spatial and temporal mesh size by a factor of 2 yields changes in the terminal cilia-driven flow rate of about 5% (under spatial mesh refinement) and 1% (under temporal mesh refinement), see Figure 4. We choose the regularization parameter ϵ in (5) to be 0.05. A smaller value of $\epsilon = 0.02$ yields change in the terminal cilia-driven flow rate of about 4%. Therefore, we consider the discretization scheme to have numerically converged. Note that the size of the computational box and thus the distance between neighboring cilia is relatively large, meaning the interactions between different cilia are neglected. In fact, doubling the computational box in the x-direction yields a change of flow rate of about 2%.
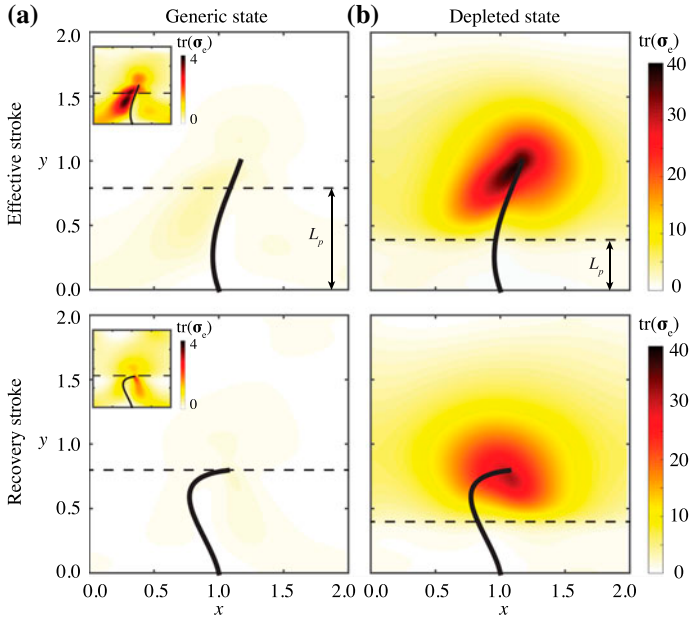
Figure 5. Elastic stress energy. Contour plots of the stress energy $\mathrm{tr}(\sigma_e)$ in (a) generic ($L_p = 0.8$) and (b) depleted ($L_p = 0.4$) states, shown at $t = 0.2T$ during the effective stroke and $t = 0.7T$ during the recovery stroke. Here, $\mathrm{De}_m = 5$ and $\mathrm{De}_p = 0.05$. Insets in (a) show the elastic stress energy with a small color scaling.

We consider a small Deborah number $\mathrm{De}_p = 0.05$ of the periciliary layer (nearly Newtonian) and we vary the elastic properties De_m of the mucus layer and its thickness L_m, which implies a change in the thickness of the periciliary layer L_p. The elastic viscosity fractions for periciliary layer and mucus layer are both $\alpha = 0.5$.

3. Results

We consider two states of periciliary layer thickness: $L_p = 0.8$, which we label as 'generic' because it is comparable to the average length of the cilium over its beating cycle as observed experimentally in healthy ciliary systems, and $L_p = 0.4$, which we label as depleted. In the generic state, the cilium tip penetrates into the mucus layer during the effective stroke as it pushes the mucus forward while the whole cilium moves in the periciliary layer during the recovery stroke. In the depleted state, the mucus layer covers part of the cilium at all times, even during the recovery stroke.

Figure 5 shows the contour plots of the elastic stress energy in these two states for mucus Deborah number $\mathrm{De}_m = 5$. The elastic stress energy is equal to the trace of the extra stress tensor $\mathrm{tr}(\sigma_e)$. Because the mucus layer has a longer relaxation time than the periciliary layer, the cilium in the depleted state generates higher fluid stresses (about 10 times) compared to the cilium in the
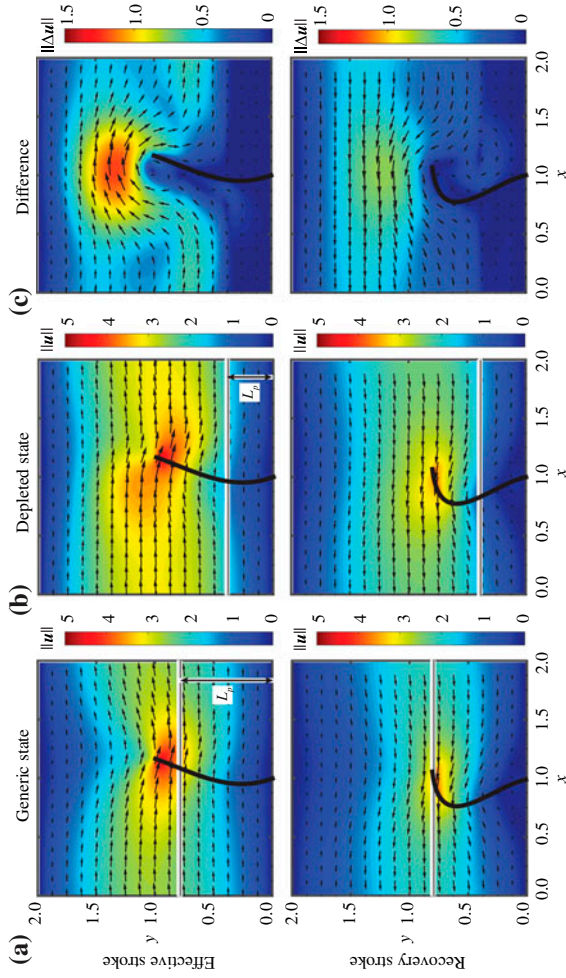
Figure 6. Velocity vector fields. Velocity fields in (a) generic state ($L_p = 0.8$) and (b) depleted state ($L_p = 0.4$). (c) The difference between the two vector fields. The colormap shows the magnitude of the fluid velocities. Here, $De_m = 5$, $De_p = 0.05$.

generic state. The spatial distribution of the elastic stress energy is also different in the two states. During the effective stroke, the stress is distributed along the cilium in the generic state (highlighted in the insets), while in the depleted state it is concentrated close to the cilium tip. During the recovery stroke, we observe larger regions of high stress with slower decay rate in the depleted state compared to the generic state. We next examine the effects of the elastic stress in the mucus on the fluid velocity field in both the generic and depleted environments.

3.1. Cilia-driven fluid velocity

Figure 6(a) and (b) depict the flow fields of the cilium in the generic and depleted states respectively. The fluid velocities close to the cilium are dictated by the cilium motion because of the no-slip boundary conditions. However, the decay of the flow velocities over space is affected by the elastic stress distribution. Compared to the generic state, the velocities decay slower in the depleted state because of the high level of stress energy, which means high elastic stress enhances the instantaneous flow. The velocity differences between the two states $\Delta \boldsymbol{u} = \boldsymbol{u}_{\text{depleted}} - \boldsymbol{u}_{\text{generic}}$ are shown in Figure 6(c). It shows an increase in positive flow during the effective stroke and an increase in negative flow during the recovery stroke, with the maximum difference in velocity appearing above the tip of the cilium. This instantaneous picture is not sufficient to assess the overall velocity difference between the generic and depleted states. For that, we evaluate the time averaged flow fields over one beating cycle, as discussed next.

Figure 7(a) shows the time averaged flow fields $\langle \boldsymbol{u} \rangle = \frac{1}{T} \int_0^T \boldsymbol{u} \mathrm{d}t$. In the generic state, the velocity field averaged over one cycle shows a single vortex-like structure below the cilium tip. On the other hand, $\langle \boldsymbol{u} \rangle$ in the depleted state shows two counter-rotating vortex-like structures. Particularly, the vortex structure at the front end (left) of the cilium rotates counter-clockwise, generating a back flow above the cilium tip in this location. That is, the generic state favors an asymmetric flow structure while the depleted state is characterized by a symmetric flow. Symmetry here is detrimental to net flow and transport in the direction of the effective stroke.

We further average the velocity field in the x-direction, namely, we compute $\langle u_x \rangle = \frac{1}{D} \int_0^D \langle \boldsymbol{u} \rangle \cdot \boldsymbol{e}_x \mathrm{d}x$, with $\boldsymbol{e}_x$ being the unit vector pointing to the x-direction. The average velocity profiles are depicted in Figure 7(b) and correspond to nonlinear shear profiles. The results of a benchmark computation in which the periciliary layer takes up the entire channel (no mucus) are shown in dashed lines. We will refer to this benchmark computation as the *control case*. In the generic state, the velocity $\langle u_x \rangle$ is almost identical to that of the control case for $y < 0.8$ (periciliary layer) and faster than that of the control state for $y > 0.8$ (mucus layer), with max $(\langle u_x \rangle)_{\text{generic}} = 0.22$. This is because the flow during the effective stroke in the generic state is enhanced by the elastic stress due to the presence of the mucus layer, while the flow during the recovery stroke remains almost the same as the control case since the cilia motion is always in the periciliary layer
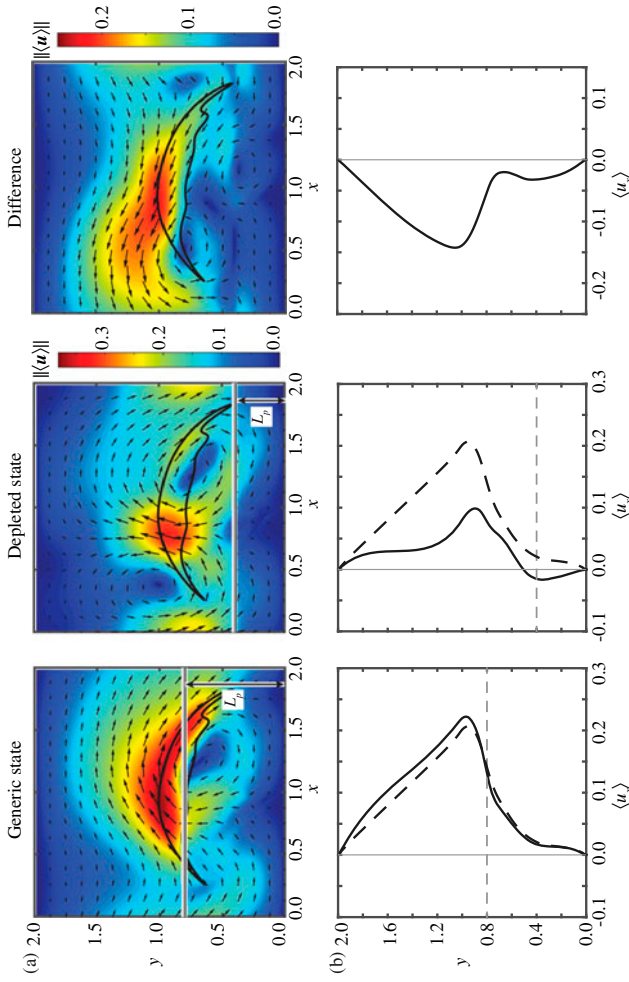
Figure 7. Flow velocity averaged over one cilia beating cycle. (a) Mean velocity fields over one cycle. The closed loops represent the trajectories of the cilium tip over one cycle. (b) Mean flow profiles in x-direction as functions of y. The black dashed curves represent the flow profile of a control state where there is no mucus ($L_p = 2.0$). The light grey dashed lines denote the interface between the mucus/periciliary layers.
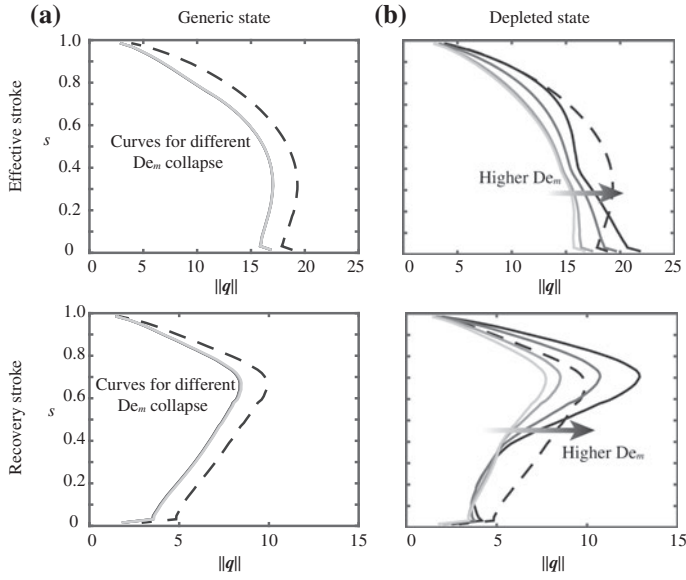
Figure 8. Internal cilia torques. Internal torques in (a) generic ($L_p = 0.8$) and (b) depleted ($L_p = 0.4$) states as functions of the arclength along the cilium for Deborah numbers $De_m = 1, 2, 5, 10$. Snapshots during the effective ($t = 0.2$) and recovery ($t = 0.7$) strokes. The dashed curves represent the results of the control case with no mucus ($L_p = 2.0$).

during recovery stroke. In other words, the presence of mucus layer enhances the flow in the effective stroke, but not the flow in the recovery stroke. In the depleted state, the flow velocity lags behind the control case for all y and, unlike the generic and control states, the flow is negative in the periciliary layer. The highest mean velocity in the depleted state is $\max(\langle u_x \rangle)_{\text{depleted}} = 0.10$, that is, $\max(\langle u_x \rangle)$ drops by over 50% from the generic. This drop in fluid transport can be attributed to the higher stress energy in the depleted state, which makes the mucus layer "stiffer" and solid like, thus hindering fluid velocity and flow transport.

3.2. Cilia internal moments and power requirements

We now evaluate the internal moments required in order for the cilia to perform the prescribed beating kinematics in both the generic and depleted conditions. As mentioned in the introduction, we assume that the beating kinematics is not affected by the thickness of the mucus layer or its elastic properties. The internal bending moments q generated by each cilium are obtained using the Kirchhoff model for an elastic filament as done in Eloy & Lauga (2012) and Guo, Nawroth, Ding, and Kanso (2014), which yields $q = Bt'' \times t + t \times \int_s^l F(\tilde{s}, t) d\tilde{s}$. Here, B is the dimensionless bending rigidity of the cilium, which we set to $B = 6.54 \times 10^{-4}$ as done in Eloy & Lauga (2012) and Guo et al. (2014), t is the unit tangent to

the cilium and the prime superscript $(\cdot)'$ represents derivative with respect to arclength s ($t'' = \partial^2 t / \partial s^2$).

Figure 8 depicts the magnitude of the internal bending moments $\|q\|$ as a function of the arclength s at two snapshots corresponding to $t = 0.2T$ during the effective stroke and $t = 0.7T$ during the recovery stroke. Figure 8(a) shows the values of $\|q\|$ in the generic state ($L_p = 0.8$) for four different values of $\text{De}_m = 1, 2, 5, 10$ compared to the control case (no mucus, dashed line) and Figure 8(b) compares the depleted state ($L_p = 0.4$, $\text{De}_m = 1, 2, 5, 10$) to the control case. Interestingly, in the generic state, the magnitude $\|q\|$ of the internal moments is independent of De_m and it takes smaller values than those in the absence of mucus (dashed line). That is to say, in the generic state and within the considered range of Deborah numbers, the internal moments required to perform the cilia beating kinematics are independent of the elastic properties of the mucus; and the same cilia beating kinematics require weaker internal moments in the presence of mucus than in its absence. The latter can be explained as a result of the interplay between the elastic properties of the fluid and the oscillatory motion of the cilia. Elasticity causes the fluid to "react" in the opposite direction once the applied forces are released. Therefore, at each reversal in the cilium motion from effective to recovery stroke and vice versa, the elastic reaction of the fluid tends to reinforce the reversal in the cilium motion, thus requiring the cilium to exert smaller forces on the fluid and resulting in smaller internal moments along the cilium. In the healthy state, the cilium tip penetrates the mucus layer only during part of the effective stroke (roughly 20% of the beating period), giving the elastic energy in the mucus enough time to relax and diffuse. Higher De_m does not seem to affect the stored elastic energy. On the other hand, in the depleted state, the required internal moments increase as a function of the mucus Deborah number and exceed the internal moments of the control case at $\text{De}_m = 5$ and 10. In the depleted state, the cilium is partially covered by the mucus at all times and the elastic stress has no time to relax and diffuse. As the Deborah number increases, the mucus becomes more stiff with little difference in the elastic energy between the effective and recovery strokes (Figure 5). This causes the system to loose the favorable interplay observed in the generic state between fluid elasticity and oscillatory cilia kinematics and requires higher internal moments for the cilium to complete its beating cycle.

The average power $\langle P \rangle$ expended internally by the cilium is equal to the power consumed by the internal moments q. Namely, one has

$$\langle P \rangle = \langle \int_0^L \max\left(0, q \cdot \mathbf{\Omega}\right) \mathrm{d}s \rangle, \tag{8}$$

where $\mathbf{\Omega} = \left(\|\dot{t}\| / \|t \times \dot{t}\|\right) t \times \dot{t}$ is the angular velocity vector and the dot represents derivative with respect to time ($\dot{t} = \partial t / \partial t$). Negative work is not taken into account because the cilium does not harvest energy from the ambient

flow (Eloy & Lauga, 2012). Since the internal moment required in the generic state is lower than that in the control case (no mucus), the resulting power is lower as well ($\langle P \rangle = 72.5$ in the generic state vs. 81 in the control case). This reduction in power requirement is consistent with the analysis of Lauga Lauga (2007), where he examined analytically the swimming motion of a small amplitude waving sheet in weakly-viscoelastic fluids. Lauga showed that it is energetically beneficial to swim in a fluid that has some elasticity, compared to a Newtonian fluid with the same viscosity. The power requirement in the depleted state with $\text{De}_m > 8$ is higher than that of the control case ($\langle P \rangle > 81$). In this case, Lauga's assumption of weak viscoelasticity is no longer valid.

3.3. *Effects of mucus layer on flow transport, power and efficiency*

We study the effects of the Deborah number De_m and thickness L_m of the mucus layer on the mean flow transport $\langle Q \rangle$, mean power expenditure $\langle P \rangle$ and efficiency η of the cilia. The total flow transported by the cilia in the channel is equal to the flow across any plane at constant x (a direct result of flow incompressibility). That is to say, the flow rate at any given time is given by $Q(t) = \int_0^L \boldsymbol{u}(0, y, t) \cdot \boldsymbol{e}_x \mathrm{d}y$. Averaging over one cycle, we get the mean flow rate

$$\langle Q \rangle = \frac{1}{T} \int_0^T \int_0^L \boldsymbol{u}(0, y, t) \cdot \boldsymbol{e}_x \mathrm{d}y \mathrm{d}t. \qquad (9)$$

Given $\langle Q \rangle$ and $\langle P \rangle$, we define the cilia transport efficiency as

$$\eta = \mu l^{-3} \langle Q \rangle^2 / \langle P \rangle. \qquad (10)$$

This definition of efficiency is consistent with that employed in Eloy & Lauga (2012) and Osterman & Vilfan (2011).

We vary the Deborah number of the mucus layer De_m from 1 to 10. Figure 9(a) shows the rate of flow transport as a function of the De_m for four distinct values of the periciliary layer thickness: $L_p = 0.4, 0.6, 0.8$, and 1. The values of $L_p = 0.4$ and 0.6 correspond to depleted conditions where the mucus layer penetrates into the periciliary space. Evidently, the effects of the mucus elasticity depends highly on the thickness of the mucus layer. Higher elasticity increases the flow rate in the generic states while decreases the flow rate in the depleted states. The flow rates of the generic states are higher than the control case (no mucus, dashed line) while those of the depleted states are lower. In fact, the flow rate of the depleted state $L_p = 0.4$ is only 20% of the generic flow rates ($L_p = 0.8$) at $\text{De}_m = 10$. These findings are consistent with the results of Teran et al. Teran et al. (2010), where they showed that compared to the viscous case, elasticity can be beneficial to the swimming of a sperm cell for a range of Deborah number and detrimental to the swimming motion if the Deborah number is too high. Further, Figure 9(a) also shows that for a given thickness of the periciliary layer,
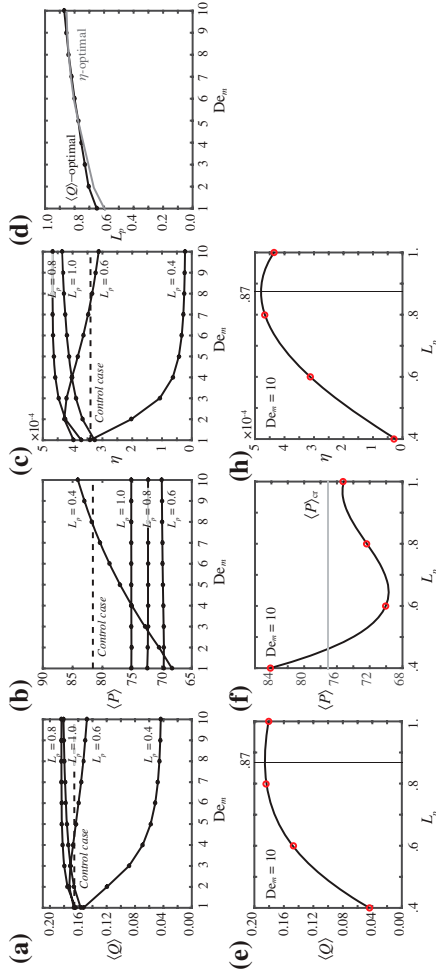
Figure 9. Cilia performance in terms of the periciliary layer thickness L_p and mucus relaxation time De_m. (a) mean flow rates, (b) mean internal powers, and (c) transport efficiencies for different periciliary layer thicknesses as functions of the relaxation time of the mucus layer. Horizontal dashed lines show the results of the control case of no mucus ($L_p = 2.0$). (d) $\langle Q \rangle$- and η-optimal values of L_p as a function of De_m. (e) mean flow rates, (f) mean internal powers, and (h) transport efficiencies as functions of periciliary layer thickness L_p for $De_m = 10$. Results are interpolated by cubic spline functions. Grey vertical lines show the periciliary layer thicknesses with the highest flow rate and transport efficiency. $\langle P \rangle_{cr}$ represents the (presumed) energy budget of cilia.

the flow rates plateau for $De_m \approx 10$, suggesting that the transport performance is robust to further changes in viscoelastic properties of the mucus layer.

The mean power $\langle P \rangle$ expended by the cilium in one cycle is depicted in Figure 9(b). Clearly, for $L_p \geq 0.8$ the power expenditure is almost independent of the mucus Deborah number. The power expenditure increases slowly with De_m for $L_p = 0.6$ and dramatically for $L_p = 0.4$. That is to say, the depleted states are characterized not only by lower flow rates $\langle Q \rangle$ but also by higher power requirements. Therefore, when limited by the energy budget $\langle P \rangle_{cr}$ of the cilium in biological or engineered systems, the cilium may not be able to complete the beating cycle once the required power exceeds that budget.

Without access to the energy budget of biological cilia, we assume that the cilia have enough power to complete the prescribed beating cycle and compute the transport efficiencies (see Figure 9(c)). The curves exhibit similar trends as the flow rates $\langle Q \rangle$. In the generic states, higher efficiencies are observed for higher Deborah numbers. In the depleted states, the efficiencies decrease with increasing Deborah numbers. In particular, at $De_m = 10$, the efficiency of $L_p = 0.4$ is only 5% of the efficiency of $L_p = 0.8$. We further plot the values of L_p that maximize $\langle Q \rangle$ and η vs. the mucus Deborah number De_m in Figure 9(d). Clearly, the optimal L_p increases from 0.6 to 0.9 as De_m increases from 1 to 10 but at a decreasing rate of change for larger De_m. That is to say, for larger De_m, the optimal periciliary layer thickness seems to level off and is not very sensitive to the further changes in De_m.

Finally, we highlight the dependence of the performance metrics $\langle Q \rangle$, $\langle P \rangle$ and η on the thickness L_p of the periciliary layer for a fixed value of $De_m = 10$. The flow rate $\langle Q \rangle$ is not a monotonic function of L_p (Figure 9(e)). It is largest for $L_p = 0.87$, for which the efficiency η is also largest (Figure 9(h)). That is, $L_p = 0.87$ is the optimal value of the periciliary layer thickness. This value is close to the value $L_p = 0.8$, which we labeled as generic state, where the thickness of the periciliary layer is comparable to the average cilia length. On the other hand, the required power reduces gradually when L_p decreases from 1 to 0.6, but increases sharply when $L_p < 0.6$ (see Figure 9(f)). An increase in the mucus layer L_m and a decrease in the periciliary thickness L_p may require higher powers than those affordable by the cilium $\langle P \rangle_{cr}$, thus preventing it from completing its beating cycle, which may lead to decreased transport performance and even complete failure in their transport function.

4. Discussion

Mucociliary clearance in the lung serves to effectively transport inhaled toxic molecules and undesirable particles away from the tissue surfaces, thus shielding the airways from potentially infectious agents. Disruptions in the ciliary apparatus, whether due to a genetic disorder or acquired causes, are directly linked to infection and disease such as CF and COPD. In these diseased conditions,

the mucociliary system is characterized by a depletion of the watery periciliary layer underlying the mucus layer. Clinical evidence connects the periciliary layer depletion to reduced rates of mucus clearance (Fahy & Dickey, 2010; Boucher, 2007). In fact, in vivo analyses of wild-type (healthy) and CF murine nasal airway surface liquid thickness show that CF decreases the airway surface liquid height from 7 μm to 4 μm, with periciliary layer thickness decreased almost by half from 4 μm to 2.5 μm (Tarran et al., 2001).

In this work, we developed a novel computational model to study mucociliary transport in a microfluidic channel consisting of a mucus layer (viscoelastic fluid) atop a periciliary layer (nearly-viscous fluid). We systematically varied the viscoelastic properties and thickness of the mucus layer to emulate healthy and diseased conditions. The representative diseased state has a periciliary layer thickness half of the representative healthy state, which is consistent with experimental observations (Tarran et al., 2001). We assessed cilia performance in terms of three metrics: flow transport, internal power expended by the cilia, and transport efficiency. We found that, compared to a control case with no mucus, a healthy mucus layer enhances cilia performance in all three metrics. That is to say, a layer of mucus atop a healthy periciliary layer not only improves flow transport but it does so at an energetic advantage for the cilia. Further, in healthy environments, increasing the Deborah number of the mucus layer enhances transport efficiency. In contrast, in diseased environments where the periciliary layer is depleted, mucus hinders transport and larger Deborah numbers reduce transport efficiency further. This decrease in efficiency is accompanied by an increase in the internal torques and power needed to complete the cilia beating cycle. Cilia therefore may not be able to beat at all if the required power is higher than the power afforded by the cilia internal machinery - this is consistent with clinical observations that link thin periciliary layers to cilia failure and dysfunction (Fahy & Dickey, 2010). It is worth noting here that the transport efficiency we obtained in the diseased state of a depleted periciliary layer $L_p = 0.4$ is only 5% of the value of the transport efficiency obtained in the healthy state of a periciliary layer thickness $L_p = 0.8$. This decrease in performance in the diseased state is accompanied by larger elastic stresses at the cilia tips and by two counter-rotating vortex-like structures below the cilia tips. The symmetry of these dipolar vortex structures is detrimental to net transport.

Our modeling framework systematically couples mucociliary transport to the parameters of the mucus layer. It establishes variations in the flow transport in response to perturbations in the mucus and periciliary layers, regardless of the physiological mechanisms that bring this about. Here, a few comments on the model advantages and limitations are in order:

(i) Our underlying assumption throughout this work was that the beating kinematics is not affected by the thickness of the mucus layer or its elastic properties. This framework is useful to compare the performance of the

unchanged cilia kinematics under various mucus conditions. We found that cilia performance is enhanced in the presence of a healthy mucus layer than in the control case of no mucus, and diminished in diseased environments when the periciliary layer is depleted. A future extension of the present study would be to allow the cilia beat kinematics to change dynamically in response to changes in the mucus environment. Such complementary approach would provide valuable insights into the effects of diseased environments on changes in the cilia beating patterns.

(ii) All cilia in this study are beating in synchrony, as ensured by the periodic boundary conditions in the x-direction. In reality, cilia beat in an orchestrated metachronal wave. In a previous work that does not explicitly account for the mucus layer, we showed that compared to beating in synchrony, a metachronal beat can result in as much as 6 times higher flow velocity for this particular cilia beating pattern (Guo et al., 2014). Taking this as a guideline, we scale the dimensionless average flow rate in the healthy condition $\langle Q \rangle / L_y = 0.09$ by the characteristic length $l_c = 6 \times 10^{-6}$ m and time $t_c = 1/15$ s reported in Fulford & Blake (1986) for the cilia beating pattern we considered in this study. The resulting estimate of the flow rate under healthy conditions is about 48.6 μm/s. Our estimate is congruent with the estimate obtained in Smith et al. (2007) and shows good agreement to various experimental measurements. In particular, experimental flow rates in the range 70–92μm/s were reported in ICRP & I. C. on Radiological Protection (1994) for tracheal transport of healthy subjects and in the range 67–333μm/s in Salathe, O'Riordan, and Wanner (1997) using less invasive measurement technique which yield lower flow rates. More recently, a flow rate of 39.2 μm/s was reported in Matsui, Randell, Peretti, Davis, and Boucher (1998).

(iii) Mucus layers are characterized by large Deborah numbers, of order 10 − 100 in healthy environments and even larger in diseased states (Lauga, 2007; Gilboa & Silberberg, 1976). Here, we varied the Deborah number De_m from 1 to 10 to establish a trend of how performance depends on De_m. We found that, in healthy environments, the transport rates increase with increasing De_m and reach a plateau as De_m approaches 10, whereas under diseased conditions, the transport rates decrease with increased De_m before reaching their plateau value (Figure 9). We also found that the internal moments along the cilia are not very sensitive to De_m under healthy conditions, but sharply increase with De_m when the periciliary layer is depleted. These findings justify the choice of the range of De_m considered in this study. In the future, larger De_m will be considered, which will render the system of equations 'stiff' and more challenging to solve computationally, requiring the use of a fully implicit fluid solver.

(iv) Our results are based on two-dimensional (2D) computations and 2D cilia beating kinematics. We used this 2D set-up to better illustrate the main

ideas and for easier visualization of the resulting flows. In this set-up, a cilium should be thought of as a 'wall' of synchronously beating cilia in the third z-direction (perpendicular to the (x, y)-plane). Compared to full 3D simulations, this set-up tends to overestimate the flow rate generated by cilia beatings, as well as the elastic energy stored in the fluid. It is worth noting that the computational framework we used is general and can be easily extended to include 3D cilia beating patterns, albeit at an increased computational cost.

(v) For simplicity, our model uses no-slip boundary conditions for the lower and upper boundary of the channel. Future work will consider more biologically relevant scenarios of a mucus layer with free surface condition or with cilia on both walls to emulate the cross-section of narrow tubes.

The two main results obtained from this study – the fact that a healthy mucus layer enhances the performance of mucociliary systems and that a depleted periciliary layer can be directly linked to diminished transport and cilia dysfunction through excessive demands on cilia internal moments – serve to complement ongoing research on understanding cilia-related diseases and to direct future studies. In conjunction with its role in understanding cilia-related diseases, the quantitative model we presented in this work could play important roles in the design and use of microfluidic devices in health-related cilia research. Indeed, a novel and exciting research direction in *in vitro* cell cultures lies in the development of engineered ciliated tissues in microfluidic chips, so called 'organs-on-chips', as the next-generation platforms for basic research, drug development, and diagnostics (Benam et al., 2015). Traditionally, the clinical use of *in vitro* cell cultures in health-related research on respiratory tissues and mucociliary transport (Seybold et al., 1990; Wanner et al., 1996) has been mostly qualitative and lacking a direct translation to clinical readouts. Organs-on-chips aim to provide clinically relevant metrics of ciliated tissue health by recapitulating and quantifying essential structure–function relationships (Nawroth & Parker, 2013), thereby achieving better predictions of disease mechanisms and treatment options in humans compared to traditional cell culture and animal models (Huh et al. 2010; Bhatia & Ingber, 2014). Our three quantitative measures of cilia transport performance can be applied to experimental data obtained from cilia-on-chip systems, thus opening the door to direct quantitative comparisons of *in vitro* healthy and diseased cilia conditions. Quantitative models such as the one presented here will be important tools for understanding the link between tissue-engineered ciliated organs and functional outcomes.

Another future direction of this work that is directly relevant to infectious disease of the airways is to determine what is required by a beneficial or pathogenic bacterial cell that colonizes the airway surfaces to resist or to work within the healthy environment of mucociliary clearance. Clearly to successfully colonize the ciliated surface, such cells must have developed mechanisms to avoid

mucociliary clearance. Most research has focused on the chemical properties of the bacteria-tissue interactions, see, e.g. McFall-Ngai (2014) and references therein, whereas several recent studies in biofluid mechanics have considered bacterial motility in otherwise still viscoelastic environments (Thomases & Guy (2014); Teran et al., 2010; Lauga, 2007; Qin, Gopinath, Yang, Gollub, & Arratia, 2015; Patteson, Gopinath, Goulian, & Arratia, 2015). However, the mechanical strategies employed by motile bacterial cells in complex environments such as in healthy and diseased mucociliary clearance remain an open research problem.

Finally, we note that in addition to their importance in clinical applications, the efficiency of biological cilia in pumping and mixing fluids at very small scales provided an attractive paradigm for fluid manipulation by artificial cilia at the micron scale (Evans et al., 2007; Khatavkar, Anderson, den Toonder, & Meijer, 2007; den Toonder et al., 2008; Vilfan et al., 2010).

Also, self-propelled microrobots by flagellar or ciliary activities are being proposed as revolutionary devices in the field of minimally invasive medicines (Nelson, Kaliakatsos, & Abbott, 2010; Peyer, Zhang, & Nelson, 2013). The quantitative model we presented in this study for assessing cilia performance in complex environments could serve as an important design tool in such microfluidic applications.

Disclosure statement

No potential conflict of interest was reported by the authors.

References

Barton, C., & Raynor, S. (1967). Analytical investigation of cilia induced mucous flow. *The Bulletin of Mathematical Biophysics, 29*, 419–428.

Benam, K. H., Dauth, S., Hassell, B., Herland, A., Jain, A., Jang, K.-J., ... Ingber, D. E. (2015). Engineered in vitro disease models. *Annual Review of Pathology: Mechanisms of Disease, 10*, 195–262.

Bhatia, S. N. & Ingber, D. E. (2014). Microfluidic organs-on-chips. *Nature Biotechnology, 32*, 760–772.

Boucher, R. C. (2004). New concepts of the pathogenesis of cystic fibrosis lung disease. *European Respiratory Journal, 23*, 146–158.

Boucher, R. C. (2007). Evidence for airway surface dehydration as the initiating event in cf airway disease. *Journal of Internal Medicine, 261*, 5–16.

Brennen, C., & Winet, H. (1977). Fluid mechanics of propulsion by cilia and flagella. *Annual Review of Fluid Mechanics, 9*, 339–398.

Brooks, E. R. & Wallingford, J. B. (2014). Multiciliated cells. *Current Biology, 24*, R973–R982.

Button, B., Cai, L.-H., Ehre, C., Kesimer, M., Hill, D. B., Sheehan, J. K., ... Rubinstein, M. (2012). A periciliary brush promotes the lung health by separating the mucus layer from airway epithelia. *Science, 337*, 937–941.

Chang, W., Giraldo, F., & Perot, B. (2002). Analysis of an exact fractional step method. *Journal of Computational Physics, 180*, 183–199.

Chatelin, R., & Poncet, P. (2016). A parametric study of mucociliary transport by numerical simulations of 3d non-homogeneous mucus. *Journal of Biomechanics, 49*, 1772–1780.

Chopra, S. K., Taplin, G. V., Simmons, D. H., & Elam, D. (1977). Measurement of mucociliary transport velocity in the intact mucosa. *CHEST Journal, 71*, 155–158.

Chorin, A. J. (1968). Numerical solution of the navier-stokes equations. *Mathematics of Computation, 22*, 745–762.

Chrispell, J., Cortez, R., Khismatullin, D., & Fauci, L. (2011). Shape oscillations of a droplet in an oldroyd-b fluid. *Physica D: Nonlinear Phenomena, 240*, 1593–1601.

Chrispell, J., Fauci, L., & Shelley, M. (2013). An actuated elastic sheet interacting with passive and active structures in a viscoelastic fluid. *Physics of Fluids, 25*, e1002167.

Comer, D. M., Elborn, J. S., & Ennis, M. (2012). Comparison of nasal and bronchial epithelial cells obtained from patients with copd. *PLOS ONE, 7*, e32924.

Cone, R. A. (2009). Barrier properties of mucus. *Advanced Drug Delivery Reviews, 61*, 75–85.

Davenport, J. R., & Yoder, B. K. (2005). An incredible decade for the primary cilium: A look at a once-forgotten organelle. *American Journal of Physiology-Renal Physiology, 289*, F1159–F1169.

Del Bigio, M. R. (1995). The ependyma: A protective barrier between brain and cerebrospinal fluid. *Glia, 14*, 1–13.

Del Donno, M., Bittesnich, D., Chetta, A., Olivieri, D., & Lopez-Vidriero, M. T. (2000). The effect of inflammation on mucociliary clearance in asthma: An overview. *CHEST Journal, 118*, 1142–1149.

den Toonder, J., Bos, F., Broer, D., Filippini, L., Gillies, M., de Goede, J., ... Anderson, P. (2008). Artificial cilia for active micro-fluidic mixing. *Lab on a Chip, 8*, 533–541.

Dillon, R. H., Fauci, L. J., Omoto, C., & Yang, X. (2007). Fluid dynamic models of flagellar and ciliary beating. *Annals of the New York Academy of Sciences, 1101*, 494–505.

Ding, Y., Nawroth, J. C., McFall-Ngai, M. J., & Kanso, E. (2014). Mixing and transport by ciliary carpets: a numerical study. *Journal of Fluid Mechanics, 743*, 124–140.

Dreyfus, R., Baudry, J., Roper, M. L., Fermigier, M., Stone, H. A., & Bibette, J. (2005). Microscopic artificial swimmers. *Nature, 437*, 862–865.

Eelkema, R., Pollard, M. M., Vicario, J., Katsonis, N., Ramon, B. S., Bastiaansen, C. W., & Feringa, B. L. (2006). Molecular machines: Nanomotor rotates microscale objects. *Nature, 440*, 163–163.

Eloy, C. & Lauga, E. (2012). Kinematics of the most efficient cilium. *Physical Review Letters, 109*, 038101.

Evans, B. A., Shields, A. R., Carroll, R. L., Washburn, S., Falvo, M. R., & Superfine, R. (2007). Magnetically actuated nanorod arrays as biomimetic cilia. *Nano Letters, 7*, 1428–1434.

Fahy, J. V., & Dickey, B. F. (2010). Airway mucus function and dysfunction. *New England Journal of Medicine, 363*, 2233–2247.

Fauci, L. J., & Dillon, R. (2006). Biofluidmechanics of reproduction. *Annual Review of Fluid Mechanics, 38*, 371–394.

Fletcher, C. (2012). *Computational techniques for fluid dynamics 2: Specific techniques for different flow categories*. New York, NY: Springer Science & Business Media.

Fulford, G. R., & Blake, J. R. (1986). Muco-ciliary transport in the lung. *Journal of Theoretical Biology, 121*, 381–402.

Gilboa, A., & Silberberg, A. (1976). In situ rheological characterization of epithelial mucus. *Biorheology, 13*, 59–65.

Guo, H., Nawroth, J. C., Ding, Y., & Kanso, E. (2014). Cilia beating patterns are not hydrodynamically optimal. *Physics of Fluids, 26*, 091901.

Hogg, J. C. (2004). Pathophysiology of airflow limitation in chronic obstructive pulmonary disease. *The Lancet, 364*, 709–721.

Huh, D., Matthews, B. D., Mammoto, A., Montoya-Zavala, M., Hsin, H. Y., & Ingber, D. E. (2010). Reconstituting organ-level lung functions on a chip. *Science, 328*, 1662–1668.

ICRP, & I. C. on Radiological Protection. (1994). *ICRP Publication 66: Human Respiratory Tract Model for Radiological Protection*, Number 66. New York, NY: Elsevier Health Sciences.

Jayathilake, P. G., Le, D. V., Tan, Z., Lee, H. P., & Khoo, B. C. (2015). A numerical study of muco-ciliary transport under the condition of diseased cilia. *Computer Methods in Biomechanics and Biomedical Engineering, 18*, 944–951.

Jayathilake, P. G., Tan, Z., Le, D. V., Lee, H. P., & Khoo, B. C. (2012). Three-dimensional numerical simulations of human pulmonary cilia in the periciliary liquid layer by the immersed boundary method. *Computers & Fluids, 67*, 130–137.

Khaderi, S., Craus, C., Hussong, J., Schorr, N., Belardi, J., Westerweel, J., Prucker, O., Rühe, J., Den Toonder, J., & Onck, P. (2011). Magnetically-actuated artificial cilia for microfluidic propulsion. *Lab on a Chip, 11*, 2002–2010.

Khatavkar, V. V., Anderson, P. D., den Toonder, J. M., & Meijer, H. E. (2007). Active micromixer based on artificial cilia. *Physics of Fluids, 19*, 083605.

Kirby, B. J. (2010). *Micro-and nanoscale fluid mechanics: Transport in microfluidic devices*. New York, NY: Cambridge University Press.

Larson, R. G. (1999). *The structure and rheology of complex fluids*. New York, NY: Oxford University Press.

Lauga, E. (2007). Propulsion in a viscoelastic fluid. *Physics of Fluids, 19*, 083104.

Lee, W. L., Jayathilake, P. G., Tan, Z., Le, D. V., Lee, H. P., & Khoo, B. C. (2011). Muco-ciliary transport: effect of mucus viscosity, cilia beat frequency and cilia density. *Computers & Fluids, 49*, 214–221.

Li, W.-E., Chen, W., Ma, Y.-F., Tuo, Q.-R., Luo, X.-J., Zhang, T., ... Liu, Q.-H. (2012). Methods to measure and analyze ciliary beat activity: Ca2+ influx-mediated cilia mechanosensitivity. *Pflügers Archiv-European Journal of Physiology, 464*, 671–680.

Li, Z., Favier, J., D'Ortona, U., & Poncet, S. (2016). An immersed boundary-lattice boltzmann method for single-and multi-component fluid flows. *Journal of Computational Physics, 304*, 424–440.

Livraghi, A., & Randell, S. H. (2007). Cystic fibrosis and other respiratory diseases of impaired mucus clearance. *Toxicologic Pathology, 35*, 116–129.

Lyons, R. A., Saridogan, E., & Djahanbakhch, O. (2006). The reproductive significance of human fallopian tube cilia. *Human Reproduction Update, 12*, 363–372.

Mark, D., Haeberle, S., Roth, G., von Stetten, F., & Zengerle, R. (2010). Microfluidic lab-on-a-chip platforms: requirements, characteristics and applications. *Chemical Society Reviews, 39*, 1153–1182.

Masoud, H., & Alexeev, A. (2011). Harnessing synthetic cilia to regulate motion of microparticles. *Soft Matter, 7*, 8702–8708.

Matsui, H., Randell, S. H., Peretti, S. W., Davis, C. W., & Boucher, R. C. (1998). Coordinated clearance of periciliary liquid and mucus from airway surfaces. *Journal of Clinical Investigation, 102*, 1125.

McFall-Ngai, M. (2014). Divining the essence of symbiosis: Insights from the squid-vibrio model. *PLOS Biology, 12*, e1001783.

Mirzadeh, Z., Han, Y.-G., Soriano-Navarro, M., García-Verdugo, J. M., & Alvarez-Buylla, A. (2010). Cilia organize ependymal planar polarity. *The Journal of Neuroscience, 30*, 2600–2610.

Mitran, S. M. (2007). Metachronal wave formation in a model of pulmonary cilia. *Computers & structures, 85*, 763–774.

Montenegro-Johnson, T. D., Smith, D. J., & Loghin, D. (2013). Physics of rheologically enhanced propulsion: Different strokes in generalized stokes. *Physics of Fluids, 25*, 081903.

Nawroth, J. C., & Parker, K. K. (2013). Design standards for engineered tissues. *Biotechnology Advances, 31*, 632–637.

Nelson, B. J., Kaliakatsos, I. K., & Abbott, J. J. (2010). Microrobots for minimally invasive medicine. *Annual Review of Biomedical Engineering, 12*, 55–85.

O'Callaghan, C., Sikand, K., & Rutman, A. (1999). Respiratory and brain ependymal ciliary function. *Pediatric Research, 46*, 704–704.

Osterman, N., & Vilfan, A. (2011). Finding the ciliary beating pattern with optimal efficiency. *Proceedings of the National Academy of Sciences, 108*, 15727–15732.

Patteson, A., Gopinath, A., Goulian, M., & Arratia, P. (2015). Running and tumbling with e coli in polymeric solutions. *Scientific Reports, 5*, 15761.

Peskin, C. S. (1972). Flow patterns around heart valves: a numerical method. *Journal of Computational Physics, 10*, 252–271.

Peskin, C. S. (2002). The immersed boundary method. *Acta Numerica, 11*, 479–517.

Peyer, K. E., Zhang, L., & Nelson, B. J. (2013). Bio-inspired magnetic swimming microrobots for biomedical applications. *Nanoscale, 5*, 1259–1272.

Qin, B., Gopinath, A., Yang, J., Gollub, J., & Arratia, P. (2015). Flagellar kinematics and swimming of algal cells in viscoelastic fluids. *Scientific Reports, 5*(9190).

Randell, S. H., & Boucher, R. C. (2006). Effective mucus clearance is essential for respiratory health. *American Journal of Respiratory Cell and Molecular Biology, 35*, 20–28.

Rogers, D. F. (2004). Airway mucus hypersecretion in asthma: An undervalued pathology? *Current Opinion in Pharmacology, 4*, 241–250.

Rogers, D. F. (2005). Mucociliary dysfunction in copd: effect of current pharmacotherapeutic options. *Pulmonary Pharmacology & Therapeutics, 18*, 1–8.

Roma, A. M., Peskin, C. S., & Berger, M. J. (1999). An adaptive version of the immersed boundary method. *Journal of Computational Physics, 153*, 509–534.

Ross, S. M. (1971). *A wavy wall analytical model of muco-ciliary pumping* (PhD thesis), Johns Hopkins University.

Salathe, M., O'Riordan, T. & Wanner, A. (1997). Mucociliary clearance. *The Lung: Scientific Foundations* (pp. 2295–2308). Philadelphia: Lippencott-Raven Inc.

Sanderson, M. J., & Sleigh, M. A. (1981). Ciliary activity of cultured rabbit tracheal epithelium: Beat pattern and metachrony. *Journal of Cell Science, 47*, 331–347.

Seybold, Z. V., Mariassy, A. T., Stroh, D., Kim, C. S., Gazeroglu, H., & Wanner, A. (1990). Mucociliary interaction in vitro: Effects of physiological and inflammatory stimuli. *Journal of Applied Physiology, 68*, 1421–1426.

Seys, L. J., Verhamme, F. M., Dupont, L. L., Desauter, E., Duerr, J., Agircan, A. S., ... Bracke, K. R. (2015). Airway surface dehydration aggravates cigarette smoke-induced hallmarks of copd in mice. *PLOS ONE, 10*, e0129897.

Simonnet, C., & Groisman, A. (2005). Two-dimensional hydrodynamic focusing in a simple microfluidic device. *Applied Physics Letters, 87*, 114104.

Smith, D. J., Gaffney, E. A., & Blake, J. R. (2007). A viscoelastic traction layer model of muco-ciliary transport. *Bulletin of Mathematical Biology, 69*, 289–327.

Smith, D. J., Gaffney, E. A., & Blake, J. R. (2008). Modelling mucociliary clearance. *Respiratory Physiology & Neurobiology, 163*, 178–188.

Smith, D. J., Gaffney, E. A. & Blake, J. R. (2009). Mathematical modelling of cilia-driven transport of biological fluids. *Proceedings of the Royal Society of London A: Mathematical, Physical and Engineering Sciences* (pp. rspa20090018). London: The Royal Society.

Stone, H. A., Stroock, A. D., & Ajdari, A. (2004). Engineering flows in small devices: microfluidics toward a lab-on-a-chip. *Annual Review of Fluid Mechanics, 36*, 381–411.

Taira, K., & Colonius, T. (2007). The immersed boundary method: A projection approach. *Journal of Computational Physics, 225*, 2118–2137.

Tarran, R., Grubb, B. R., Parsons, D., Picher, M., Hirsh, A. J., Davis, C. W., & Boucher, R. C. (2001). The cf salt controversy: In vivo observations and therapeutic approaches. *Molecular cell, 8*, 149–158.

Taylor, G. I. (1951). Analysis of the swimming of microscopic organisms. *Proceedings of the Royal Society of London Series A, 209*, 447–461.

Teran, J., Fauci, L., & Shelley, M. (2010). Viscoelastic fluid response can increase the speed and efficiency of a free swimmer. *Physical Review Letters, 104*, 038101.

Teran, J. M., & Peskin, C. S. (2009). Tether force constraints in stokes flow by the immersed boundary method on a periodic domain. *SIAM Journal on Scientific Computing, 31*, 3404–3416.

Thomases, B. (2011). An analysis of the effect of stress diffusion on the dynamics of creeping viscoelastic flow. *Journal of Non-Newtonian Fluid Mechanics, 166*, 1221–1228.

Thomases, B., & Guy, R. D. (2014). Mechanisms of elastic enhancement and hindrance for finite-length undulatory swimmers in viscoelastic fluids. *Physical Review Letters, 113*, 098102.

Tierno, P., Golestanian, R., Pagonabarraga, I., & Sagués, F. (2008). Controlled swimming in confined fluids of magnetically actuated colloidal rotors. *Physical Review Letters, 101*, 218304.

Van Delden, R. A., Ter Wiel, M. K., Pollard, M. M., Vicario, J., Koumura, N., & Feringa, B. L. (2005). Unidirectional molecular motor on a gold surface. *Nature, 437*, 1337–1340.

Vilfan, M., Potocnik, A., Kavcic, B., Osterman, N., Poberaj, I., Vilfan, A., & Babic, D. (2010). Self-assembled artificial cilia. *Proceedings of the National Academy of Sciences, 107*, 1844–1847.

Wanner, A., Salathé, M., & O'Riordan, T. G. (1996). Mucociliary clearance in the airways. *American Journal of Respiratory and Critical Care Medicine, 154*, 1868–1902.

Wielpütz, M. O., Weinheimer, O., Eichinger, M., Wiebel, M., Biederer, J., Kauczor, H.-U., ... Puderbach, M. (2013). Pulmonary emphysema in cystic fibrosis detected by densitometry on chest multidetector computed tomography. *PLOS ONE, 8*, e73142.

Zhao, B., Moore, J. S., & Beebe, D. J. (2001). Surface-directed liquid flow inside microchannels. *Science, 291*, 1023–1026.